energies

MDPI

Article

Power-Sharing Control Strategy for an Open-End Winding Dual-Inverter Photovoltaic–Energy Storage System Based on Decoupled Modulation

Wenqing Cui [1], Peiyu Chen [1], Bin Xu [1], Zhiyong Gan [1], Yufei Liu [2] and Guozheng Zhang [2,*]

[1] Electric Power Research Institute, State Grid Tianjin Electric Power Company, Tianjin 300384, China; wcui_ncepu@163.com (W.C.); peiyu_chen@tju.edu.cn (P.C.); xubinsdu@163.com (B.X.); tj_ganzhiyong@163.com (Z.G.)
[2] School of Electrical Engineering, Tiangong University, Tianjin 300387, China; liuyufei@tiangong.edu.cn
* Correspondence: zhanggz@tju.edu.cn

Abstract

The open-winding dual inverter topology has the advantages of a multilevel output, high DC voltage utilization, large modulation freedom, and easy fault tolerance, and is widely used in photovoltaic grid-connected systems. The open-winding photovoltaic–energy-storage converter system studied in this paper adopts this topology. The system consists of photovoltaic and energy-storage units, and the two converters can independently deliver active power to the grid when the DC-bus voltages on both sides are balanced. To achieve active-power regulation and distribution between the photovoltaic side and the energy-storage side, this paper constructs a mathematical model of the open-winding dual-inverter photovoltaic–energy-storage system and proposes a power-allocation strategy for steady-state operation. Compared with the conventional SPWM, the proposed strategy introduces a reference-voltage allocation layer before the SPWM modules, enabling flexible power sharing while retaining the simple implementation of the conventional SPWM. The proposed strategy effectively guarantees the operational stability and grid-connected power quality of the photovoltaic–energy-storage converter. Finally, its feasibility and effectiveness are verified through simulation analysis and experimental testing.

Keywords: dual inverter; DC bus voltage balancing; open-winding transformer; photovoltaic power generation system

Check for updates

Academic Editors: Shoaib Ahmed Shaikh, Antonio D'angola and Waquar Khokhar

Received: 28 July 2026
Revised: 22 August 2026
Accepted: 25 August 2026
Published: 28 August 2026

Copyright: © 2026 by the authors. Licensee MDPI, Basel, Switzerland. This article is an open access article distributed under the terms and conditions of the Creative Commons Attribution (CC BY) license.

1. Introduction

With the continued advancement of the low-carbon energy transition, integrated grid-connected photovoltaic–energy-storage systems have been widely developed and applied [1]. As the power converter is a key interface in photovoltaic–energy-storage systems, converter topology and control have become important research topics in grid-connected applications [2,3].

Conventional two-level converters exhibit high grid-current harmonics and a large dv/dt in high-power grid-connected photovoltaic—energy-storage applications [4]. In contrast, the T-type three-level topology has two switches connected in reverse series between the midpoint and the output [5]. The T-type three-level converter reduces the voltage stress on the inner switches and provides an additional output-voltage level, thereby reducing the dv/dt and the filtering requirement compared with a conventional two-level converter [6]. However, is still difficult to promote the application of the T-type

three-level topology due to the existence of the problem of the unbalanced voltage at the midpoint, facing the high-level bus voltage and other working conditions [7]. In order to improve the midpoint voltage imbalance problem, new multilevel topologies such as the cascaded H-bridge (CHB) and modular multilevel converter (MMC) have attracted attention in recent years. The cascaded H-bridge (CHB) converter avoids the capacitor equalization problem fundamentally by virtue of the unitized series voltage divider [8]. However, it relies on bulky and costly multi-winding industrial frequency phase-shifter transformers. The modular multilevel converter (MMC) structure is also more complex and has a large number of components [9], but it is self-powered by a sub-module suspension capacitor, which frees it from the constraints of a phase-shifter transformer and allows for a bidirectional flow of energy [10]. However, MMC control is comparatively complex, and the rapid variations in photovoltaic generation or the frequent charging/discharging of the storage unit can increase the submodule-capacitor voltage fluctuations [11].

Against this background, the open-winding topology with unique structural features has gradually become a research hotspot. This topology adopts two conventional two-level converters connected to both ends of the primary winding of the transformer [12]. With the appropriate modulation, the two inverters can synthesize an equivalent three-level voltage waveform across the open-end winding. Compared with an MMC, the dual-inverter open-end-winding topology can reduce the modulation and control complexity; compared with some isolated CHB implementations, it can also reduce the reliance on bulky phase-shifting transformers. In addition, it avoids the neutral-point balancing issue inherent to neutral-point-based three-level converters [13]. In addition, a wider variety of voltage vector combinations and switching combinations are available, significantly increasing the degree of control freedom [14]. The open-winding topology, by virtue of its advantages such as the high voltage utilization and ease of control, on the one hand, means the application of this technology in new energy vehicles can improve energy utilization efficiency [15]. On the other hand, photovoltaic–energy storage converters are widely used in isolated islands and remote areas where there is sufficient light [16].

At present, the open-winding topology is mainly used in large-capacity grid-connected photovoltaic projects with two power supply modes: the common DC bus or independent DC bus [17,18]. For common-DC-bus systems, zero-sequence-current suppression methods based on voltage-vector reselection have been proposed to suppress the circulating zero-sequence current while coordinating the active-power contributions of the two inverters [19]. With isolated DC buses, variations in photovoltaic generation and battery operating conditions may lead to unequal DC-link operating conditions and unbalanced power availability. Existing studies have therefore introduced power-coordination or compensation strategies to redistribute the inverter power contributions and maintain stable grid-connected operation [20].

Combined with the above situation, this paper proposes a power allocation strategy based on the voltage balance of the two buses. In the face of the energy shortage or excess caused by extreme weather, the power allocation is carried out according to the appropriate ratio, so as to realize the reasonable distribution of power between the two sides of PV and energy storage.

2. Modelling and Voltage Space-Vector Analysis of the Open-End Winding Photovoltaic–Energy-Storage Converter

2.1. Topology of the Open-End Winding Photovoltaic–Energy-Storage Converter

The topology of the photovoltaic and storage converter system based on the open-winding transformer connection is shown in Figure 1 (the photovoltaic panels and storage batteries are equivalent to a DC power source with voltage V_{dc}. The dashed boxes indicate

the boundaries of VSI-1, VSI-2, and the transformer winding sections.). VSI-1 and VSI-2 denote the photovoltaic-side and energy-storage-side converters, respectively. The neutral point of the transformer primary winding is open, and the two ends of each phase winding are connected to the corresponding phase terminals of VSI-1 and VSI-2. C_1 and C_2 are the DC-link capacitors of VSI-1 and VSI-2, respectively.

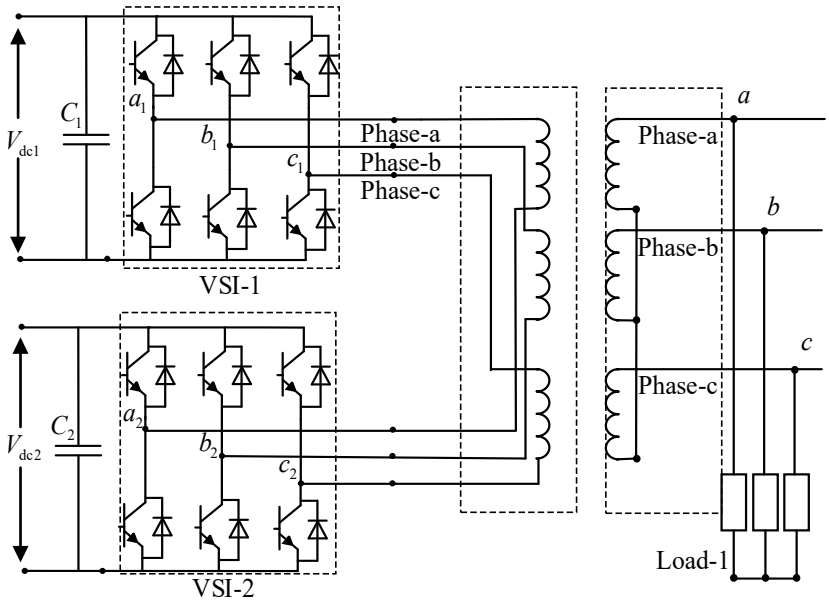


Figure 1. Model of open-end winding photovoltaic–energy storage converter.

The PV-side DC/DC converter employs the perturb-and-observe method to achieve maximum power point tracking. The PV voltage and current are sampled to calculate the output power, and the operating-voltage reference is adjusted according to the observed power variation. When the PV power increases, the perturbation direction is maintained; otherwise, it is reversed. The resulting maximum available PV power is provided to the EMS for determining the PV-side power reference and the power-sharing coefficient.

In practical applications, the PV array and battery are connected to the two isolated DC buses through a PV-side DC/DC converter and a bidirectional battery-side DC/DC converter, respectively. The two DC/DC converters regulate V_{dc1} and V_{dc2} to the same rated reference. Therefore, the balanced DC-bus condition adopted in this paper refers to the regulated DC-link voltages rather than the varying terminal voltages of the PV array and battery. Small voltage deviations and parameter mismatches mainly reduce the modulation margin and power-sharing accuracy. Stable operation can be maintained by the current feedback controller within the linear modulation region, whereas the power-sharing coefficient and total power reference should be limited when a large DC-link voltage deviation occurs.

The transformer primary winding phase voltage can be expressed as follows:

$$\begin{cases} v_{a1a2} = v_{a1g1} - v_{a2g2} + v_{g1g2} \\ v_{b1b2} = v_{b1g1} - v_{b2g2} + v_{g1g2} \\ v_{c1c2} = v_{c1g1} - v_{c2g2} + v_{g1g2} \end{cases} \quad (1)$$

where v_{a1g1}, v_{b1g1}, and v_{c1g1} are the three-phase phase voltages of VSI-1, respectively; similarly, v_{a2g2}, v_{b1g2}, and v_{c2g2} are the three-phase phase voltages of VSI-2, respectively, and $\boldsymbol{V}_{ref1}$ is the common mode voltage. In this topology, the voltage vector $\boldsymbol{V}_{ref2}$ acting on the primary winding of the transformer is obtained by synthesizing the voltage vector

$\boldsymbol{V}_{\text{ref}}$ from the output of the photovoltaic converter and that from the output of the energy storage converter, which is defined as follows:

$$\boldsymbol{V}_{\text{ref}} = \frac{2}{3}\left(v_{\text{a1a2}} + v_{\text{b1b2}}\text{e}^{j\frac{2\pi}{3}} + v_{\text{c1c2}}\text{e}^{j\frac{4\pi}{3}}\right) \tag{2}$$

The three-phase currents i_x (x = A, B, C) at the primary side of the transformer can be expressed as follows:

$$\begin{cases} i_{\text{A}} = I\cos(\theta - \varphi) \\ i_{\text{B}} = I\cos(\theta - \varphi - 2\pi/3) \\ i_{\text{C}} = I\cos(\theta - \varphi + 2\pi/3) \end{cases} \tag{3}$$

where I denotes the current amplitude, θ is the electrical angle, and φ is the power factor angle. The reference voltage V_x (x = A, B, C) of the photovoltaic–energy storage inverter is expressed as follows:

$$\begin{cases} V_{\text{A}} = \left(\dfrac{2m}{\sqrt{3}}\right)\cos\theta \\ V_{\text{B}} = \left(\dfrac{2m}{\sqrt{3}}\right)\cos\left(\theta - \frac{2\pi}{3}\right) \\ V_{\text{C}} = \left(\dfrac{2m}{\sqrt{3}}\right)\cos\left(\theta + \frac{2\pi}{3}\right) \end{cases} \tag{4}$$

The modulation index is defined as follows:

$$m = \sqrt{3}\left|V_{\text{ref}}\right|/(2V_{\text{dc}}) \tag{5}$$

In this paper, the *i-j* coding method is introduced to define the switching state of the open-winding photovoltaic–energy storage converter system. i and j, with values ranging from 0 to 7, represent the basic voltage vectors of the converter VSI-1 and VSI-2 outputs, respectively. The correspondence between the converter power device turn-on and turn-off states and the output basic voltage vector is shown in Table 1. If the current switching state of the system is (1,4), then the switching state of the three-phase power device of VSI-1 is (1,0,0); i.e., the upper bridge arm power device of phase A is on, and the lower bridge arm power device is off, and the upper bridge arm power device of phases B and C is off, and the lower bridge arm power device is on. The switching state of the three-phase power device of VSI-2 is (0,1,1); i.e., the upper bridge arm power device of phase A is off, and the lower bridge arm power device is on. The lower bridge arm power device of phase A is turned off and the lower bridge arm power device is turned on, while the upper bridge arm power device of phase B and C is turned on and the lower bridge arm power device is turned off.

Table 1. Switching state relationship between inverter and power devices.

Inverter Switching State	Power Device Switching State	Inverter Switching State	Power Device Switching State
0	000	4	011
1	100	5	001
2	110	6	101
3	010	7	111

2.2. 180° Decoupled Modulation

In the open-winding photovoltaic storage converter system, the photovoltaic converter and the energy storage converter can each output 8 switching states, corresponding to the 7 basic voltage vectors in the space vector diagram (shown in Figure 2), so the system has a total of 8^2 = 64 switching state combinations, corresponding to the 19 basic voltage vectors

in the space vector diagram (shown in Figure 3, where the numerical symbols 0, 1, 2, and 3 represent the basic vector magnitude; 0 represents a zero vector, 1 represents a small vector, 2 represents a medium vector, and 3 represents a large vector).

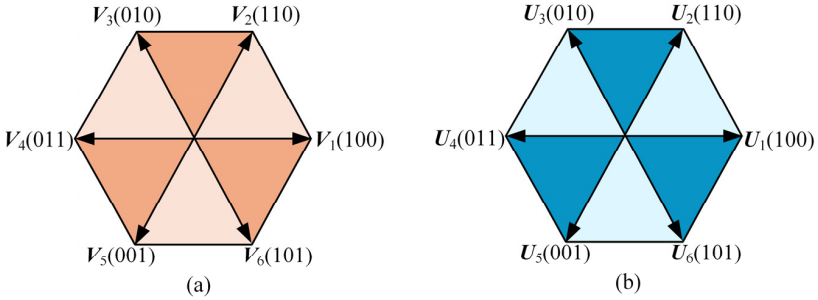


Figure 2. Inverter voltage vector space diagrams: (**a**) VSI-1; (**b**) VSI-2.

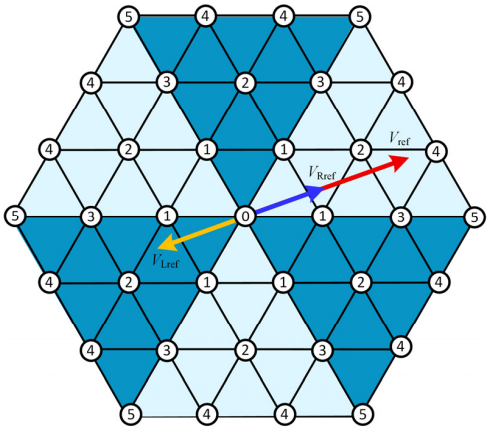


Figure 3. Voltage vector space diagram of the dual inverter. The red, blue, and yellow arrows represent $\boldsymbol{V}_{\mathrm{ref}}$, $\boldsymbol{V}_{\mathrm{Rref}}$ and $\boldsymbol{V}_{\mathrm{Lref}}$, respectively.

In order to reduce the complexity of the modulation algorithm, this paper adopts the space voltage vector modulation method based on 180° decoupling. The core idea of this method is to decompose the total reference voltage vector $\boldsymbol{V}_{\mathrm{ref}}$ into two sub-reference voltage vectors $\boldsymbol{V}_{\mathrm{ref1}}$ and $\boldsymbol{V}_{\mathrm{ref2}}$, which are modulo equal and 180° different from each other, that is,

$$\begin{cases} \boldsymbol{V}_{\mathrm{ref1}} = \dfrac{1}{2}\boldsymbol{V}_{\mathrm{ref}} \\ \boldsymbol{V}_{\mathrm{ref2}} = -\dfrac{1}{2}\boldsymbol{V}_{\mathrm{ref}} \end{cases} \tag{6}$$

For two inverters with identical ratings and balanced DC-link voltages, minimizing $\max\{\alpha, 1-\alpha\}$ gives $\alpha = 0.5$. Thus, both inverters have the same modulation index and the maximum linear modulation margin. Equation (6) represents this balanced operating point, while Section 3.3 generalizes the allocation factor from 0.5 to k for flexible power sharing.

Compared with the 120° decoupling modulation method, the 180° decoupling modulation method enables the synthetic reference voltage vector of the system to reach any position in the space vector diagram shown in Figure 3, which effectively improves the DC bus voltage utilization. And the common mode voltage generated by the PV converter and the energy storage converter cancels each other, which can reduce the conduction EMI at the switching frequency multiplier, and reduce the size and cost of the filter. Moreover, the switching losses of the two converters are the same, so there is no need for a separate heat dissipation design. Compared with the coupled modulation method, both converters can be modulated by the standard two-level modulation method without a complex vector synthesis and solution, and the modulation method is simple.

For switching states i and j of VSI-1 and VSI-2, respectively, the resultant voltage vector applied to the open winding is expressed as $\boldsymbol{V}_{ij} = \boldsymbol{V}_i - \boldsymbol{V}_\mathrm{j}$. Therefore, the two inverters provide 64 switching-state combinations. Owing to vector redundancy, these combinations correspond to 19 distinct voltage-vector positions. The resultant vector plane is divided into six main sectors, denoted as Sector I–Sector VI, with each sector spanning 60°. After the 180° decomposition, the two sub-reference vectors are synthesized independently using the adjacent active vectors and zero vectors of the corresponding sectors.

Taking Sector I as an example, when $\boldsymbol{V}_{\mathrm{ref1}}$ is located between $\boldsymbol{V}_1$[100] and $\boldsymbol{V}_2$[110], these two adjacent active vectors and the zero vectors $\boldsymbol{V}_0$[000] and $\boldsymbol{V}_7$[111] are selected. Under the 180° decomposition, $\boldsymbol{V}_{\mathrm{ref2}}$ is located in the opposite Sector IV and is synthesized using $\boldsymbol{U}_4$[011], $\boldsymbol{U}_5$[001], and the corresponding zero vectors. The dwell times are calculated according to the volt-second balance principle. Symmetrical switching sequences, such as 000→100→110→111→110→100→000 for VSI-1, are employed to reduce switching transitions and waveform distortion. Therefore, the proposed decoupled modulation transforms the switching-state selection of the dual inverter into two independent conventional two-level SPWM processes.

3. Control Design of an Open-Winding Photovoltaic–Energy Storage Converter

3.1. Current Inner Loop Closed-Loop Control Design

In the open-end-winding topology, VSI-1 and VSI-2 are connected in series through the transformer primary winding and, therefore, carry the same phase current. In order to achieve a stable grid connection and subsequent energy scheduling of the system, this common current has to be accurately controlled in a closed-loop manner.

The control system is formulated in the synchronous dq reference frame. The grid-side reactive power is limited to zero, so the q-axis reference command for current control is directly set to zero ($i_\mathrm{q} = 0$), and the core of the control system is thus reduced to the univariate static-free tracking of the d-axis active current component i_d. In the control implementation, the system firstly obtains the grid voltage phase θ_{PLL} through the phase-locked loop (PLL), and then converts the collected three-phase AC currents into the d-axis current feedback quantity i_d by using the coordinate transformation.

Under grid-voltage-oriented control, $u_\mathrm{q} = 0$, and the active and reactive powers can be expressed as $P = 3u_\mathrm{d}i_\mathrm{d}/2$ and $Q = -3u_\mathrm{d}i_\mathrm{q}/2$, respectively. Therefore, the d-axis and q-axis currents independently regulate the active and reactive powers. In this study, i^* q is set to zero to achieve unity-power-factor operation. When reactive-power support is required, i^* q can be generated by an additional reactive-power outer loop, while the active-power allocation coefficient k remains unchanged.

The active current command i_d^*, which is converted from the global active power demand of the system, is compared with the feedback i_d, and the error is sent to the proportional-integral (PI) regulator. In order to improve the system's immunity to grid voltage disturbances and dynamic response speed, the d-axis component u_d of the grid voltage is introduced as feedforward compensation. The simplified d-axis current inner-loop control equation can be expressed as follows:

$$u_{\mathrm{d_ref}} = u_\mathrm{d} + \left(K_p + \frac{K_i}{s}\right)(i_\mathrm{d}^* - i_\mathrm{d}) \tag{7}$$

$u_{\mathrm{d_ref}}$ is the d-axis component of the synthetic reference voltage output from the current regulator, and K_p and K_i are the proportional and integral gains of the PI controller. The $u_{\mathrm{d_ref}}$ can be equivalently synthesized into the total reference voltage vector $\boldsymbol{V}_{\mathrm{ref}}$ required by the system after inverse coordinate transformation. The block diagram of the current closed-loop control structure is shown in Figure 4.

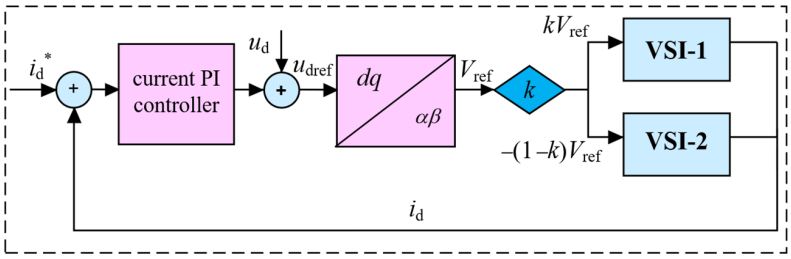


Figure 4. Block diagram of current closed-loop control structure.

3.2. Active Power Representation of the Open-Winding Photovoltaic–Energy Storage Converter System

In the open-winding topology, the currents flowing through the two inverters are equal. In order to clearly represent the energy flow of the system, a d-q synchronous rotating coordinate system is established and the grid voltage is accurately orientated to the d-axis ($u_q = 0$). Under unity-power-factor operation, the q-axis component of the grid-side current is controlled to zero ($i_q = 0$). At this time, the total active power P output from the system to the grid can be simplified and expressed as follows:

$$P = \frac{3}{2} u_d i_d \tag{8}$$

where u_d is the d-axis component of the transformer primary synthesized voltage and i_d is the d-axis component of the primary common current.

Since the synthesized voltage is applied jointly by the two inverters ($u_d = u_{d1} - u_{d2}$), it is possible to decouple the total active power into the active power components borne by each of VSI-1 and VSI-2 as follows:

$$\begin{cases} P_1 = \frac{3}{2} u_{d1} i_d \\ P_2 = \frac{3}{2} (-u_{d2}) i_d \end{cases} \tag{9}$$

From the above equations, because VSI-1 and VSI-2 share the common current i_d, the independent adjustment of P_1 and P_2 must be achieved by regulating the corresponding d-axis voltage components u_{d1} and u_{d2}.

Equation (9) describes the fundamental-frequency average active power under balanced sinusoidal operating conditions and $i_q = 0$. When a reactive current is present, the power contributions are $P_1 = 1.5(u_{d1} i_d + u_{q1} i_q)$ and $P_2 = 1.5(u_{d2} i_d + u_{q2} i_q)$. Because the complete reference voltage vectors are allocated by k, the fundamental active-power sharing relationship remains applicable when $i_q \neq 0$, provided that both converters operate in the linear modulation region. Harmonic currents introduce additional power oscillations and may cause small power-sharing errors; these harmonic components are not included in the fundamental model of Equation (9).

3.3. Power Decoupling Control Based on Vector Allocation

In an open-winding photovoltaic storage inverter system powered by an isolated equal DC source, the coupling characteristics of the grid-side currents require the system to have a precise scheduling capability for the active power flow. For this reason, a power distribution factor k is introduced in the control architecture to reconstruct the total reference voltage vector $\boldsymbol{V}_{ref}$ of the system. The reference voltage vectors of the two inverters are defined as follows:

$$\begin{cases} \boldsymbol{V}_{ref1} = k \cdot \boldsymbol{V}_{ref} \\ \boldsymbol{V}_{ref2} = -(1-k) \boldsymbol{V}_{ref} \end{cases} \tag{10}$$

It is mapped onto the d-axis voltage component of the synchronous rotating coordinate system, i.e., $u_{d1} = ku_d$ and $u_{d2} = -(1-k)u_d$. Substituting these expressions into the active power equation under the unit power factor, the output power of the two converters can be obtained as follows:

$$\begin{cases} P_1 = k \cdot P \\ P_2 = (1-k) \cdot P \end{cases} \tag{11}$$

Based on the above power allocation mathematical model, conditions of the open-winding photovoltaic storage system are determined by dynamically adjusting the control variable k:

Case 1: The PV converter and the storage converter transmit power to the grid simultaneously ($0 < k < 1$). When the system is in the grid-connected state, the variable k is set between 0 and 1. In this case, both P_1 and P_2 are positive, and the two converters jointly output active power to the grid. In the equilibrium condition ($k = 0.5$), the PV side and the storage side share the total power demand equally ($P_1 = P_2 = 0.5P$).

Case 2: The PV converter transmits power to the grid while charging the storage battery ($k > 1$). When the PV converter outputs power, and its output power is greater than the grid-side active demand (i.e., $P_1 > P$), the system adjusts the distribution coefficient so that it crosses the critical point ($k > 1$). At this point, $P_2 = (1-k)P < 0$. In this case, VSI-1 (PV side) continues to output power outward, while VSI-2 (storage side) absorbs power by virtue of the reconfigured reverse voltage vector, and feeds back the excess active power from the PV side to the storage battery through the transformer primary side.

3.4. Control Block Diagram and Core Control Flow of Photovoltaic–Energy Storage and Converter System

Based on the above control process, a block diagram of the control structure of the open-winding photovoltaic–energy storage converter system can be established, as shown in Figure 5. The total active-power command P^* is used as the outer-loop reference. The three-phase grid voltages and currents are measured at the point of connection and transformed using the PLL angle to obtain the active-power feedback P and the dq current components. Under the unit power factor condition ($i_q{}^* = 0$, $i_q = 0$), the power outer loop generates the active current of the inner loop through the PI regulator for the given $i_d{}^*$.

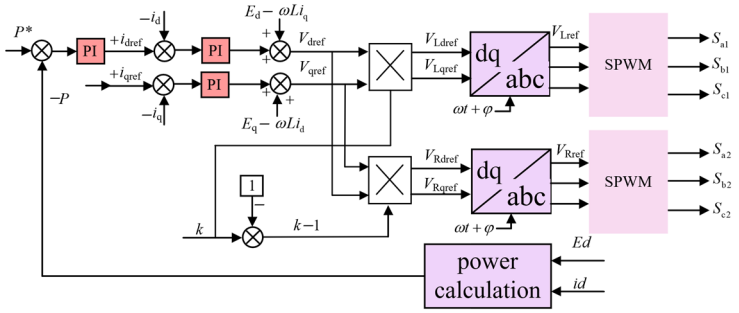


Figure 5. Photovoltaic–energy storage converter control block diagram.

This current command is transferred to the inner current loop, and the difference with the feedback quantity i_d is made through the PI regulator, and the grid voltage d-axis feed-forward quantity u_d is superimposed to suppress the fluctuation of the grid on the network side, and then the system synthetic reference voltage vector $\boldsymbol{V}_{ref}$ is obtained.

Finally, the decoupling allocation module introduces the value of k, decouples the reference voltage vector $\boldsymbol{V}_{ref}$ by 180°, generates the PV converter reference voltage $\boldsymbol{V}_{ref1}$ and the energy storage converter reference voltage $\boldsymbol{V}_{ref2}$, respectively, and then generates the converter power device driving pulses through the SPWM module.

The power-sharing coefficient k is generated by the upper-level Energy Management System (EMS), rather than directly by the MPPT or battery SOC controller. The EMS determines the reference powers of the PV and storage converters according to the total grid power command, available PV power obtained from MPPT, and battery SOC and power limits. Accordingly, k is calculated as $k = P^*\,1/P^*$, with $P^*\,2 = P^* - P^*\,1$. It is updated periodically by the EMS at a slower rate than the converter current control loop.

The upper-level EMS adopts a PV-priority dispatch rule. At each EMS update instant, the available PV power $P_{\mathrm{pv,av}}$ is compared with the total grid-power command P^*. When $P_{\mathrm{pv,av}} < P^*$ and battery discharging is permitted, the PV-side reference is set as $P_1^* = P_{\mathrm{pv,av}}$, and the storage unit supplies the remaining power. When the available PV power exceeds P^* and battery charging is permitted, the surplus PV power is transferred to the storage unit within its charging-power and SOC limits. Otherwise, the surplus PV power is curtailed.

After P_1^* is determined, the storage-side reference and allocation coefficient are calculated as $P_2^* = P^* - P_1^*$ and $k = P_1^*/P^*$, respectively. All references are limited by the converter power ratings and the modulation boundary derived in Section 4. If the available PV power and allowable battery-discharge power are insufficient, the EMS reduces the total grid-power reference to a feasible value.

The grid phase angle θ_{PLL} is extracted from the sampled three-phase grid voltage by the phase-locked loop and is used for both the abc–dq and dq–abc coordinate transformations. The PI gains are designed using pole-zero cancellation for the equivalent RL plant, with $K_{\mathrm{i}}/K_{\mathrm{p}} = R/L$. For the selected current-loop bandwidth of $f\mathrm{c} = 500$ Hz, the gains are calculated as $K_{\mathrm{p}} = 2\pi f\mathrm{c}L$ and $K_{\mathrm{i}} = 2\pi f\mathrm{c}R$. Substituting L and R gives $K_{\mathrm{p}} = 9.425$ and $K_{\mathrm{i}} = 157.08$. The resulting gain crossover frequency is approximately 500 Hz, and the phase margin is approximately 63°.

4. Power Boundary Analysis of Open-Winding Photovoltaic–Energy Storage Converters

4.1. Voltage Constraints in the Linear Modulation Region of the Inverter

In the actual operation of the open-winding photovoltaic–energy storage converter system, the selection of the power distribution coefficient k is not arbitrary, but is subject to the strict constraints of the physical parameters of the system. To avoid overmodulation, the voltage-modulation and power-transfer boundaries must be determined.

The maximum phase voltage fundamental amplitude V_{max} that the PV converter VSI-1 and the storage converter VSI-2 can output within the linear modulation region is constrained to be as follows:

$$V_{\mathrm{max}} = \frac{V_{\mathrm{dc}}}{\sqrt{3}} \tag{12}$$

Under the steady-state grid-connected condition, the total synthetic reference voltage vector magnitude at the primary side of the transformer is approximately equal to the peak grid phase voltage $\boldsymbol{V}_{\mathrm{m}}$ if the small voltage drop of the filter inductor is neglected. According to the space vector linear decoupling law derived in the previous section, the voltage vector magnitudes assigned to the two inverters are as follows:

$$\begin{cases} |\boldsymbol{V}_{\mathrm{ref1}}| = kV_m \\ |\boldsymbol{V}_{\mathrm{ref2}}| = |1-k|V_m \end{cases} \tag{13}$$

In order to ensure that the two machines operate simultaneously in the linear modulation zone, the following set of absolute value inequality equations must be satisfied simultaneously:

$$\begin{cases} k \cdot V_m \le \dfrac{V_{dc}}{\sqrt{3}} \\ |1-k| \cdot V_m \le \dfrac{V_{dc}}{\sqrt{3}} \end{cases} \tag{14}$$

4.2. Power Distribution and Regulation of Distribution Coefficients

The range of values of the power distribution factor k is influenced by both the DC bus voltage of the converter as well as the modulation index m. The output voltage vector magnitudes of the PV converter and the storage converter are as follows:

$$\begin{cases} \boldsymbol{V}_{ref1} = (1-k)m\dfrac{2V_{dc}}{\sqrt{3}} \\ \boldsymbol{V}_{ref2} = km\dfrac{2V_{dc}}{\sqrt{3}} \end{cases} \tag{15}$$

In order to ensure that the system does not overmodulate, the reference voltage amplitude of both inverters needs to be less than V_{max}. Bringing the above equation into the maximum voltage limiting condition yields the following:

$$\begin{cases} \left| km\dfrac{2V_{dc}}{\sqrt{3}} \right| \le \dfrac{V_{dc}}{\sqrt{3}} \\ \left| (1-k)m\dfrac{2V_{dc}}{\sqrt{3}} \right| \le \dfrac{V_{dc}}{\sqrt{3}} \end{cases} \tag{16}$$

Let the total regime m of the system be in the range [0, 1], and, when the system is in different regimes m, by simplifying the above inequality, the boundary of k can be determined as follows:

$$1 - \frac{1}{2m} \le k \le \frac{1}{2m} \tag{17}$$

According to this boundary condition, the relationship between the system regulation system m and the power distribution coefficient k can be obtained, as shown in Figure 6. Since the PV converter and the storage converter DC bus voltage is equal, the graph presents completely symmetrical characteristics.

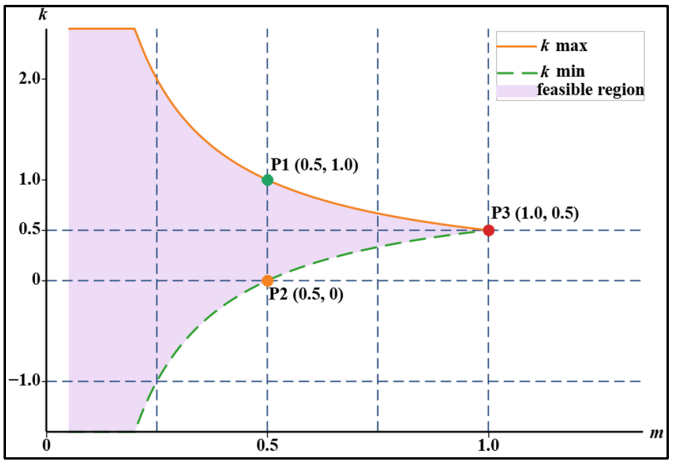


Figure 6. Photovoltaic–energy storage converter m vs. k.

For different values of the governing system m and the distribution coefficient k, the specific operating conditions of the system are as follows:

When $0 \le m \le 0.5$, the value range of the distribution coefficient k can cover the region of $k \le 0$ and $k \ge 1$. At this time, the two converters can realize the bidirectional flow of energy

between the two converters. For example, when $k > 1$, the photovoltaic side charges for the energy storage side, and, when $k < 0$, the energy flows from the energy storage side to the photovoltaic side (due to the physical constraints, this condition does not exist in practice).

When $0.5 < m < 1$, the value of k is strictly limited to the interval (0,1). At this time, both inverters must output positive active power, and both of them are in the mode of supplying power to the grid.

When the output voltage reaches the maximum, $m = 1$ and $k = 0.5$. The two converters share the total active power equally and the power-sharing ratio is no longer adjustable.

Before experimental validation, the proposed system is compared with conventional photovoltaic–energy-storage systems, as shown in Table 2. The proposed open-winding system provides an equivalent three-level output and utilizes the sum of the two DC-link voltages. Under isolated DC-source conditions, no circulating-current path exists. Moreover, active power is directly distributed through the allocation coefficient k, instead of DC-bus voltage regulation or droop/MPC-based power sharing. Unlike droop- or DC-bus-voltage-based power sharing, the proposed method directly allocates the reference-voltage vector through k without introducing an additional power-sharing control loop. It also avoids the online prediction and optimization required by MPC.

Table 2. Comparison of typical PV–energy-storage systems.

Item	Common DC-Bus System	Common AC-Bus System	Proposed Open-Winding System
Output voltage levels	Two-level	Two-level	Equivalent three-level
Effective DC voltage	V_{dc}	V_{dc}	$2V_{dc}$
Circulating current	Absent	Possible	Absent
Power sharing	DC-bus regulation	Droop/MPC	Allocation coefficient k

5. Experimental Validation and Analysis of Result

In order to verify the correctness and effectiveness of the power allocation strategy of the open-winding photovoltaic–energy storage converter system proposed in this paper, an RT-lab based experimental platform was built for testing. The experimental parameters are given in Table 3.

Table 3. Main implementation parameters of the system.

Parameters	Unit	Value
Switching Frequency	Hz	10k
Sampling Frequency	Hz	10k
Dead Time	μs	1
Transformer Rated Voltage	V	380/380
Transformer Rated Frequency	Hz	50
Equivalent Series Inductance	mH	3
Equivalent Series Resistance	Ω	0.05
DC-link Capacitors	μF	3300
DC-link Voltages	V	1200
PV Array Nominal Voltage	V	600–900
Battery Nominal Voltage	V	1000–1300
PV-Side DC/DC Input/Output Voltage	V	600–900/1200
Battery-Side DC/DC Input/Output Voltage	V	1000–1300/1200
PV-Side DC/DC Rated Power	kW	40
Battery-Side DC/DC Rated Power	kW	25

The experiments focus on the dynamic power allocation between the photovoltaic and energy-storage sides by adjusting the power-sharing coefficient k while maintaining the total grid-connected active power P_{total} essentially constant. Figures 7–9 present the

experimental waveforms under different operating conditions. The recorded quantities include the photovoltaic-side active power P_1, energy-storage-side active power P_2, total grid-connected active power P_{total}, phase-A output voltages of the two converters $v_{\text{VSI-1,A}}$ and $v_{\text{VSI-2,A}}$, differentially synthesized phase-A voltage of the open-end winding transformer v_{A}, grid-side phase-A current i_{A}, battery state of charge (SOC), and battery current i_{bat}. In addition, an FFT analysis is performed on v_{A}, and the corresponding voltage and current THD values are provided to quantitatively evaluate the grid-connected power quality during the power redistribution.

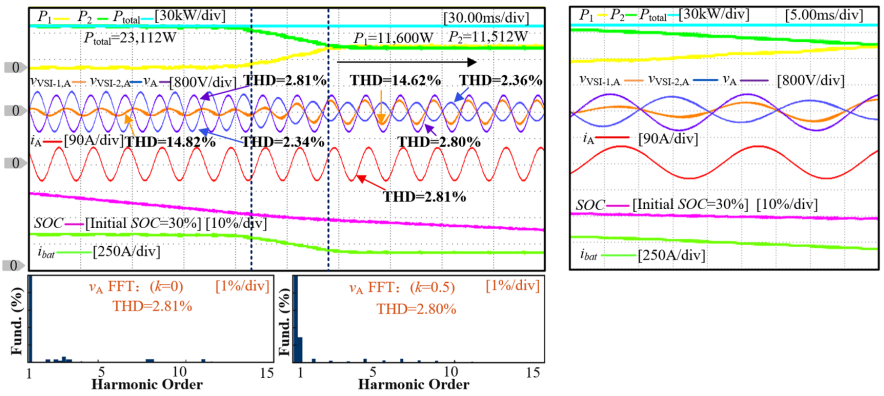


Figure 7. Photovoltaic–energy storage co-discharge condition (0 < k < 1).

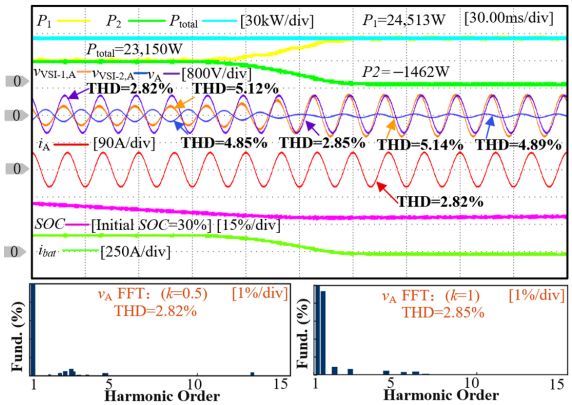


Figure 8. Photovoltaic discharge and storage inoperative conditions.

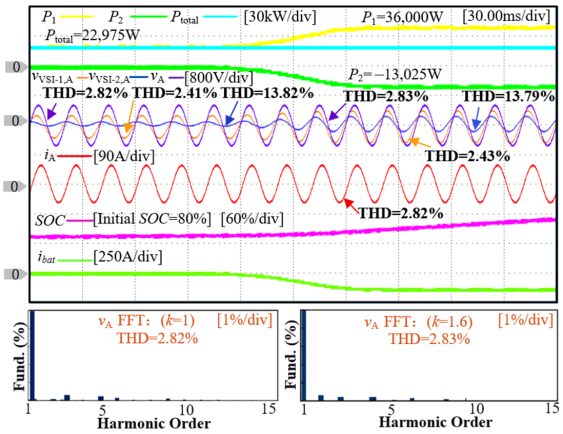


Figure 9. Photovoltaic full-load discharge energy storage and absorption working conditions.

5.1. Simultaneous Power Output from PV Converter and Storage Converter (0 < k < 1)

Figure 7 shows the experimental waveforms when the photovoltaic converter and the energy-storage converter simultaneously deliver active power to the grid. Initially,

the power-sharing coefficient is $k = 0$; the photovoltaic-side converter output power P_1 is close to zero, while the energy-storage side supplies most of the system active power, with the total grid-connected active power P_{total} remaining near 23.112 kW. Subsequently, k is adjusted from 0 to 0.5. P_1 increases smoothly while P_2 decreases synchronously. Throughout the power redistribution process, P_{total} remains essentially constant, indicating that the variation in the power-sharing coefficient primarily reconstructs the internal active-power contribution between the two converters without causing an appreciable fluctuation in the total grid-side active power.

After the system reaches a steady state at $k = 0.5$, the measured powers are $P_1 = 11.600$ kW and $P_2 = 11.512$ kW, satisfying $P_1 + P_2 = 23.112$ kW $= P_{\text{total}}$. According to the equal-power-sharing relationship at $k = 0.5$, the ideal reference power for each side is 11.556 kW. Therefore, the steady-state errors of VSI-1 and VSI-2 relative to the equal-sharing reference are approximately +0.38% and −0.38%, respectively. From the power transition shown in Figure 7, the dynamic redistribution time after k is changed from 0 to 0.5 is approximately 60 ms. Because the powers shown in the figure are active-power values averaged over a fundamental-frequency cycle, the steady-state percentage error is used to characterize power-sharing accuracy, rather than defining an additional RMS power-tracking error. The experimental results demonstrate that the proposed vector-allocation method achieves continuous, stable, and high-accuracy active-power sharing within $0 < k < 1$.

From the AC-side voltage waveforms, the power redistribution is accompanied by the reconstruction of the amplitudes and waveforms of the two converter terminal voltages. At $k = 0$, the THDs of $v_{\text{VSI-1,A}}$, $v_{\text{VSI-2,A}}$, and the synthesized voltage v_{A} are 14.82%, 2.34%, and 2.81%, respectively. At $k = 0.5$, the corresponding THDs are 14.62%, 2.36%, and 2.80%. Although the harmonic contents of the two converter terminal voltages vary with the power-sharing ratio, the THD of v_{A} changes only from 2.81% to 2.80%. The FFT results at the bottom of Figure 7 agree with these measurements, indicating that the quality of the differentially synthesized voltage at the open-end winding terminals is essentially unaffected by the change in power allocation during the reconstruction of the two reference voltage vectors.

The grid-side phase-A current i_{A} maintains a continuous, nearly sinusoidal waveform before and after the transition, with a steady-state THD of approximately 2.81%; no evident low-frequency oscillation or abrupt change is observed. The battery SOC decreases continuously from its initial value of 30%, indicating that the battery remains in the discharging state under this operating condition. As P_2 decreases from supplying most of the system power to 11.512 kW, the magnitude of the battery current i_{bat} decreases accordingly and settles to a new steady state, reflecting the corresponding reduction in the discharge power supplied by the energy-storage side.

In addition, the system efficiency was measured at the steady-state operating point of $k = 0.5$. The conversion efficiencies of VSI-1 and VSI-2 are 98.03% and 98.04%, respectively, the efficiency of the open-end winding transformer is approximately 97.72%, and the overall system efficiency is 95.80%. These results show that the proposed power-sharing strategy maintains a high energy-conversion efficiency while achieving nearly equal active-power sharing between the two sides.

5.2. The PV Converter Outputs Power to the Grid Alone

To emulate an operating scenario with sufficient solar irradiance in which the photovoltaic side gradually assumes the grid-side power demand, Figure 8 presents the experimental results as the power-sharing coefficient increases from $k = 0.5$ to $k = 1$. During the experiment, the total grid-connected active power P_{total} remains close to 23.150 kW. As k increases, the photovoltaic-side output power P_1 continuously rises, whereas the energy-storage-side

power P_2 continuously decreases, and the system gradually transitions from a coordinated photovoltaic–energy-storage power supply to a photovoltaic-dominated operating state.

Near the steady-state operating point of $k = 1$, the measured values are $P_1 = 24.513$ kW and $P_2 = -1.462$ kW. Their sum is 23.051 kW, yielding a residual of 99 W relative to $P_{\text{total}} = 23.150$ kW, which corresponds to only 0.43% of the total power. This result indicates that the practical $k = 1$ operating point lies close to the power-flow boundary at which the energy-storage side changes from forward discharge to reverse power absorption. Owing to non-ideal factors such as device losses, the power-measurement chain, and fundamental-cycle averaging, the measured P_2 is not exactly zero. Nevertheless, its magnitude is substantially smaller than the total system power; therefore, this condition can be regarded as a near-standby boundary operating point of the energy-storage side.

In terms of voltage quality, at $k = 0.5$, the THDs of $v_{\text{VSI-1,A}}$, $v_{\text{VSI-2,A}}$, and v_{A} are 5.12%, 4.85%, and 2.82%, respectively. After the transition to $k = 1$, the corresponding THDs are 5.14%, 4.89%, and 2.85%, representing changes of only 0.02, 0.04, and 0.03 percentage points, respectively. The corresponding FFT results show that the THD of v_{A} increases only slightly from 2.82% to 2.85% and remains at a low level. Although the terminal-voltage amplitudes and power-sharing ratios of the two converters change appreciably, the differentially synthesized v_{A} retains a good sinusoidal quality, demonstrating that the 180° decoupled modulation can maintain a stable synthesized-voltage quality near the power-flow boundary.

The grid current i_{A} remains continuous throughout the transition, with a steady-state THD of approximately 2.82%, and no evident current oscillation is observed. The initial battery SOC is approximately 30%. As P_2 gradually decreases, the battery current i_{bat} decreases synchronously and approaches zero, while the SOC remains essentially around its initial value over the relatively short observation interval. Because the front-end bidirectional DC/DC converter on the VSI-2 side continuously regulates the DC-bus voltage, its DC bus remains stable at 1200 V. Therefore, even when the energy-storage side approaches the standby boundary, the system maintains stable grid-connected active power and good AC-side waveform quality.

5.3. PV Full-Load Discharge Energy Storage and Absorption Conditions ($k > 1$)

To further verify the reverse power absorption by the energy-storage side and bidirectional energy transfer in the $k > 1$ region, Figure 9 presents the experimental results when the power-sharing coefficient is changed from $k = 1$ to $k = 1.6$. During the transition, the total grid-connected active power P_{total} remains close to 22.975 kW, the photovoltaic-side power P_1 increases further from a level close to the total grid-connected power, and the energy-storage-side power P_2 continues to move in the negative direction. After the system reaches a steady state at $k = 1.6$, the measured values are $P_1 = 36.000$ kW and $P_2 = -13.025$ kW, satisfying $P_1 + P_2 = 22.975$ kW $= P_{\text{total}}$. Thus, of the 36.000 kW active power generated on the photovoltaic side, 22.975 kW is delivered to the grid and the remaining 13.025 kW is transferred through the open-end winding transformer and the energy-storage-side converter to the storage unit, thereby realizing simultaneous photovoltaic grid feeding and battery charging.

From the measured steady-state powers, $P_1/P_{\text{total}} = 1.5669$ and $P_2/P_{\text{total}} = -0.5669$, corresponding to a measured equivalent power-sharing coefficient of approximately $k_{\text{eq}} = 1.567$. Compared with the commanded value $k = 1.6$, the equivalent-coefficient deviation is approximately 0.033. According to the ideal power-sharing relationship, the reference powers at $k = 1.6$ are $P_1^* = 36.760$ kW and $P_2^* = -13.785$ kW. Although a finite steady-state deviation exists between the commanded coefficient and the measured equivalent power ratio, the sum of the measured powers on the two sides remains exactly consistent with P_{total}, demonstrating that the practical system correctly realizes the power-direction reversal and energy redistribution for $k > 1$.

The voltage-harmonic results further demonstrate the differential-synthesis characteristic of the open-end winding topology. At k = 1, the THDs of $v_{VSI\text{-}1,A}$, $v_{VSI\text{-}2,A}$, and v_A are 2.41%, 13.82%, and 2.82%, respectively. After the transition to k = 1.6, the corresponding THDs are 2.43%, 13.79%, and 2.83%. The terminal-voltage THD of one converter remains approximately 13.8%, whereas the THD of the synthesized voltage v_A changes by only 0.01 percentage points, from 2.82% to 2.83%. The FFT results at the bottom of Figure 9 agree with the annotations in the main waveforms, indicating that, even under a highly asymmetric power-sharing condition, the relatively high harmonic content of an individual converter terminal voltage is not directly transferred to the differentially synthesized voltage of the open-end winding transformer.

The grid-side current i_A remains nearly sinusoidal throughout the transition from k = 1 to 1.6, with a steady-state THD of approximately 2.82%, and no evident low-frequency oscillation is observed. The initial battery SOC is 80%. After P_2 stabilizes at −13.025 kW, the battery charging current is approximately 203.7 A, the SOC exhibits a continuous increasing trend, and i_{bat} changes toward the charging direction before reaching a steady state, consistent with the direction of active-power absorption by the energy-storage side. This result demonstrates that, even with approximately 13.025 kW of reverse power transfer inside the system, the total grid-connected power remains stable at 22.975 kW, thereby achieving bidirectional energy flow without an additional power-conversion branch.

Considering the power-quality measurements in Figures 7–9 as a whole, the THD of the open-end winding differentially synthesized voltage v_A remains within 2.80–2.85% under the different power-sharing conditions, while the THD of the grid current i_A is approximately 2.81–2.82%. The measured voltage distortion is below the 5% voltage-distortion limit specified by IEEE 519 for points of common coupling below 69 kV. Under the rated-current test conditions adopted in this study, the current THD can be used as an approximate indicator of total demand distortion and is likewise below 5%. Therefore, the proposed power-sharing strategy maintains a good grid-connected power quality while enabling continuous power regulation and the reversal of the energy-storage-side power direction.

To evaluate the effect of unequal DC-link voltages, an additional experiment was conducted at k = 0.5, as shown in Figure 10. When the VSI-1 DC-link voltage decreased from 1200 V to 1150 V while the VSI-2 DC-link voltage remained at 1200 V, the power-sharing errors were approximately −2.05% and +2.05%. Nevertheless, the total grid-connected power remained stable at approximately 23.796 kW, and the synthesized-voltage THD remained approximately 2.17%. These results demonstrate that the proposed strategy remains effective under a DC-link voltage mismatch within 5%, provided that both inverters operate in the linear modulation region.

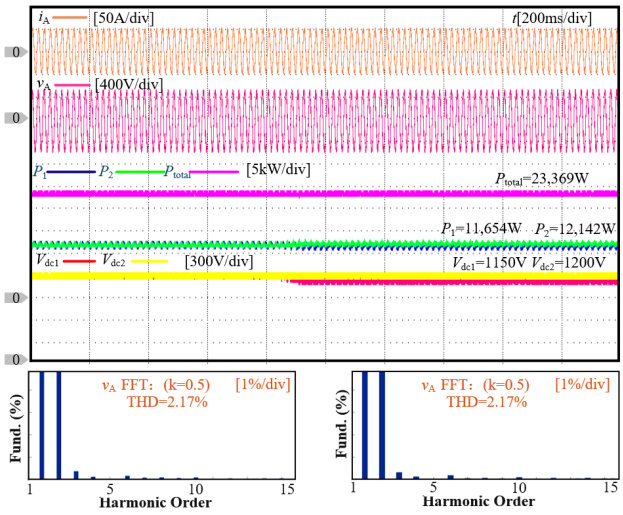


Figure 10. Experimental results under unequal DC-link voltages at k = 0.5.

6. Conclusions

In this paper, a control strategy based on the 180° decoupling of space voltage vectors and flexible active power allocation is proposed for the open-end winding photovoltaic–energy storage grid-connected converter system under the DC bus voltage balancing condition, and its steady-state characteristics and dynamic reconstruction process are verified by the RT-lab experimental platform. The following conclusions are drawn:

(1) The simplified modulation algorithm. The 180° decoupled modulation strategy is adopted to downscale the complex three-level modulation to two independent conventional two-level modulations. The method circumvents the midpoint potential imbalance problem of the conventional three-level topology, and doubles the equivalent fundamental phase voltage amplitude under the physical constraint of equal DC sources on both sides to improve the DC bus voltage utilization compared with the conventional single-inverter system.

(2) Power decoupling and bi-directional flow without additional hardware are realized. By introducing and dynamically adjusting the power allocation coefficient k, the reference voltage vectors of the bilateral converter are reconstructed, and the active power allocation between the PV side and the storage side is achieved. The system is capable of switching between PV and storage co-discharge ($0 < k < 1$), one-side standby ($k = 1$), and PV full-load discharge and storage absorption ($k > 1$), solving the problem of PV excess energy and other energy flow problems under extreme weather.

(3) Guaranteeing good grid-connected power quality. The experimental results show that the transformer primary synthesized voltage remains constant when more than 10 kW of large-capacity active power flows through the system. The grid-side phase currents remain nearly sinusoidal, with no evident low-frequency oscillation observed in the reported waveforms. The proposed control strategy ensures effective energy allocation within the photovoltaic–energy-storage system while maintaining the power quality at the grid connection point.

(4) The main contribution over conventional SPWM is the introduction of an adjustable reference-vector allocation layer before the two SPWM modules. This approach retains the simple modulation process of conventional two-level inverters while enabling flexible power sharing among PV–storage co-discharge, single-side operation, and PV-to-storage energy transfer.

Author Contributions: Conceptualization, G.Z. and W.C.; methodology, W.C. and P.C.; software, W.C.; validation, B.X.; formal analysis, Y.L.; investigation, B.X.; resources, P.C.; data curation, Z.G.; writing—original draft preparation, Y.L.; writing—review and editing, G.Z.; visualization, W.C.; supervision, P.C.; project administration, P.C.; funding acquisition, P.C. and G.Z. All authors have read and agreed to the published version of the manuscript.

Funding: This research was funded by "The Science and Technology Project of State Grid Tianjin Electric Power Company (Electric Science-S&T Project 2025-42)".

Data Availability Statement: The original contributions presented in this study are included in the article. Further inquiries can be directed to the corresponding author.

Conflicts of Interest: Author Wenqing Cui, Peiyu Chen, Bin Xu and Zhiyong Gan were employed by the company State Grid Tianjin Electric Power Company Electric Power Research Institute. The remaining authors declare that the research was conducted in the absence of any commercial or financial relationships that could be construed as a potential conflict of interest. The authors declare that this study received funding from the company The Science and Technology Project of State Grid Tianjin Electric Power Company Electric Power Research Institute. The funder was not involved in the study design; the collection, analysis, and interpretation of the data; the writing of this article; or the decision to submit it for publication.

Abbreviations

PV	Photovoltaic
ESS	Energy storage system
PWM	Pulse-width modulation
SPWM	Sinusoidal pulse-width modulation
EMI	Electromagnetic interference
MPPT	Maximum power point tracking
EMS	Energy management system
SOC	State of charge
VSI-1 and VSI-2	Voltage-source inverter 1, Voltage-source inverter 2
DC	Direct current
PLL	Phase-Locked Loop
CHB	Cascaded H-Bridge Converter
MMC	Modular Multilevel Converter

Nomenclature

V_{dc1}, V_{dc2}	DC-link voltages of VSI-1 and VSI-2
$\boldsymbol{V}_{ref}$	Total reference voltage vector
$\boldsymbol{V}_{ref1}$, $\boldsymbol{V}_{ref2}$	Reference voltage vectors of VSI-1 and VSI-2
$V_x (x = A, B, C)$	Three-phase reference voltages of the PV–ESS inverter system
φ	Power-factor angle
v_{a1g1}, v_{b1g1}, v_{c1g1}	Three-phase phase voltages of VSI-1
v_{a2g2}, v_{b2g2}, v_{c2g2}	Three-phase phase voltages of VSI-2
v_{g1g2}	Common-mode voltage
θ_{PLL}	Grid voltage angle obtained from the PLL
k	Allocation Coefficient
m	Modulation index
$v_{VSI\text{-}1,A}$	A-phase output voltage of VSI-1

References

1. Medardo, M.C.L.; Hao, Z. Three-phase interleaved bidirectional LLC resonant converter for high-efficiency PV-battery energy storage systems. In Proceedings of the 2026 2nd International Conference on Smart Energy and Control Engineering (SECE), Wenzhou, China, 10–12 April 2026.
2. Zhang, X.; Feng, G. MMC-based PV grid-connected system with SMES-battery hybrid energy storage system. *IEEE Trans. Appl. Supercond.* **2024**, *34*, 5702004. [CrossRef]
3. Maurya, B.; Sharma, S. Smart grid synchronization techniques with PV generating system and its challenges: An overview of the power sector in India. In Proceedings of the 2023 International Conference on Artificial Intelligence and Smart Communication (AISC), Greater Noida, India, 27–29 January 2023.
4. Kishore, N.; Shukla, K.; Gupta, N. A novel three-phase multilevel inverter cascaded by a three-phase two-level inverter and two single-phase boosted H-bridge inverters. In Proceedings of the 2022 IEEE PES Innovative Smart Grid Technologies–Asia (ISGT Asia), Singapore, 1–5 November 2022.
5. Li, X.; Huangfu, Y.; Wang, S.; Jin, L. Research on control and simulation of three-level T-type inverter. In Proceedings of the 2025 IEEE 8th International Electrical and Energy Conference (CIEEC), Changsha, China, 16–18 May 2025.
6. Nguyen, Q.-B.; Dung, P.C.; Vu, H.-C.; Dinh, T.N.; Tran, Q.-H. A modulated model predictive control for three-phase three-level T-type inverter. In Proceedings of the 2022 11th International Conference on Control, Automation and Information Sciences (ICCAIS), Hanoi, Vietnam, 21–24 November 2022.
7. Cai, H.; Chen, M.; Xu, D. A neutral-point voltage-balance control for three-level T-type inverters with carrier-based discontinuous PWM. In Proceedings of the 2025 Zhejiang Power Electronics Conference (ZPEC), Hangzhou, China, 22–24 August 2025.
8. Nayak, S.; Das, A.; Torres-Olguin, R.E.; D'Arco, S.; Guidi, G. Battery energy support to cascaded H-bridge converter-fed large-scale PV systems during unbalanced power generation. In Proceedings of the 2020 International Conference on Power, Instrumentation, Control and Computing (PICC), Thrissur, India, 17–19 December 2020.
9. Zhao, T.; Wang, G.; Bhattacharya, S.; Huang, A.Q. Voltage and power balance control for a cascaded H-bridge converter-based solid-state transformer. *IEEE Trans. Power Electron.* **2013**, *28*, 1523–1532. [CrossRef]

10. Deng, F.; Lü, Y.; Liu, C.; Heng, Q.; Yu, Q.; Zhao, J. Overview on submodule topologies, modeling, modulation, control schemes, fault diagnosis, and tolerant control strategies of modular multilevel converters. *Chin. J. Electr. Eng.* **2020**, *6*, 1–21. [CrossRef]
11. Haq, S.; Biswas, S.P.; Jahan, S.; Islam, M.R.; Rahman, M.A.; Mahmud, M.P.; Kouzani, A.Z. An advanced PWM technique for MMC inverter-based grid-connected photovoltaic systems. *IEEE Trans. Appl. Supercond.* **2021**, *31*, 0601605. [CrossRef]
12. An, Q.; Liu, J.; Peng, Z.; Sun, L.; Sun, L. Dual-space-vector control of open-end winding permanent-magnet synchronous motor drive fed by dual inverter. *IEEE Trans. Power Electron.* **2016**, *31*, 8329–8342. [CrossRef]
13. Zhong, L.; Hu, S. Three-phase reference-voltage-independent-control-based discontinuous modulation algorithm for open-end winding PMSM fed by dual three-level inverters with common DC bus. *IEEE Trans. Power Electron.* **2022**, *37*, 8379–8391. [CrossRef]
14. Sakurai, T.; Haga, H. Integrated dual inverter for PMSM drive systems under single-phase AC power supply. *IEEE Trans. Ind. Appl.* **2026**, *62*, 3943–3954. [CrossRef]
15. Das, T.; Halder, S.; Shah, V.A. Efficient energy management system for open-winding motor drive for electrical vehicles with hybrid energy storage systems. In Proceedings of the 2022 IEEE Global Conference on Computing, Power and Communication Technologies (GlobConPT), New Delhi, India, 23–25 September 2022.
16. Surasmi, N.L.; Shiny, G.; Vinod, B.R. Grid-integrated hybrid renewable energy system for power-quality improvement using an open-end winding transformer. In Proceedings of the 2024 International Conference on E-Mobility, Power Control and Smart Systems (ICEMPS), Thiruvananthapuram, India, 18–20 April 2024.
17. Lu, Q.; Wang, Y.; Ye, X. Zero-sequence current suppression strategy for open-winding permanent-magnet synchronous motor with common DC bus. In Proceedings of the 2020 IEEE International Conference on Applied Superconductivity and Electromagnetic Devices (ASEMD), Tianjin, China, 16–18 October 2020.
18. Matsumori, H.; Maeda, Y.; Kosaka, T.; Matsui, N.; Saha, S. Optimum PWM switching-mode selection of dual-inverter-fed open-winding IPMSM drive system for high-power premium-class EV. In Proceedings of the 2020 IEEE Energy Conversion Congress and Exposition (ECCE), Detroit, MI, USA, 11–15 October 2020.
19. Wang, B.; Zhang, X.; Cao, R. A zero-sequence steerable CBPWM strategy for eliminating zero-sequence current of dual-inverter-fed open-end winding transformer-based PV grid-tied system with common DC bus. *IEEE Access* **2020**, *8*, 81220–81231. [CrossRef]
20. Wang, B.; Zhang, X.; Song, C.; Cao, R. A new arrangement of LCL filter for dual-inverter-fed open-end winding transformer topology in PV applications. In Proceedings of the 2019 10th International Conference on Power Electronics and ECCE Asia (ICPE 2019–ECCE Asia), Busan, Republic of Korea, 27–31 May 2019.

Disclaimer/Publisher's Note: The statements, opinions and data contained in all publications are solely those of the individual author(s) and contributor(s) and not of MDPI and/or the editor(s). MDPI and/or the editor(s) disclaim responsibility for any injury to people or property resulting from any ideas, methods, instructions or products referred to in the content.